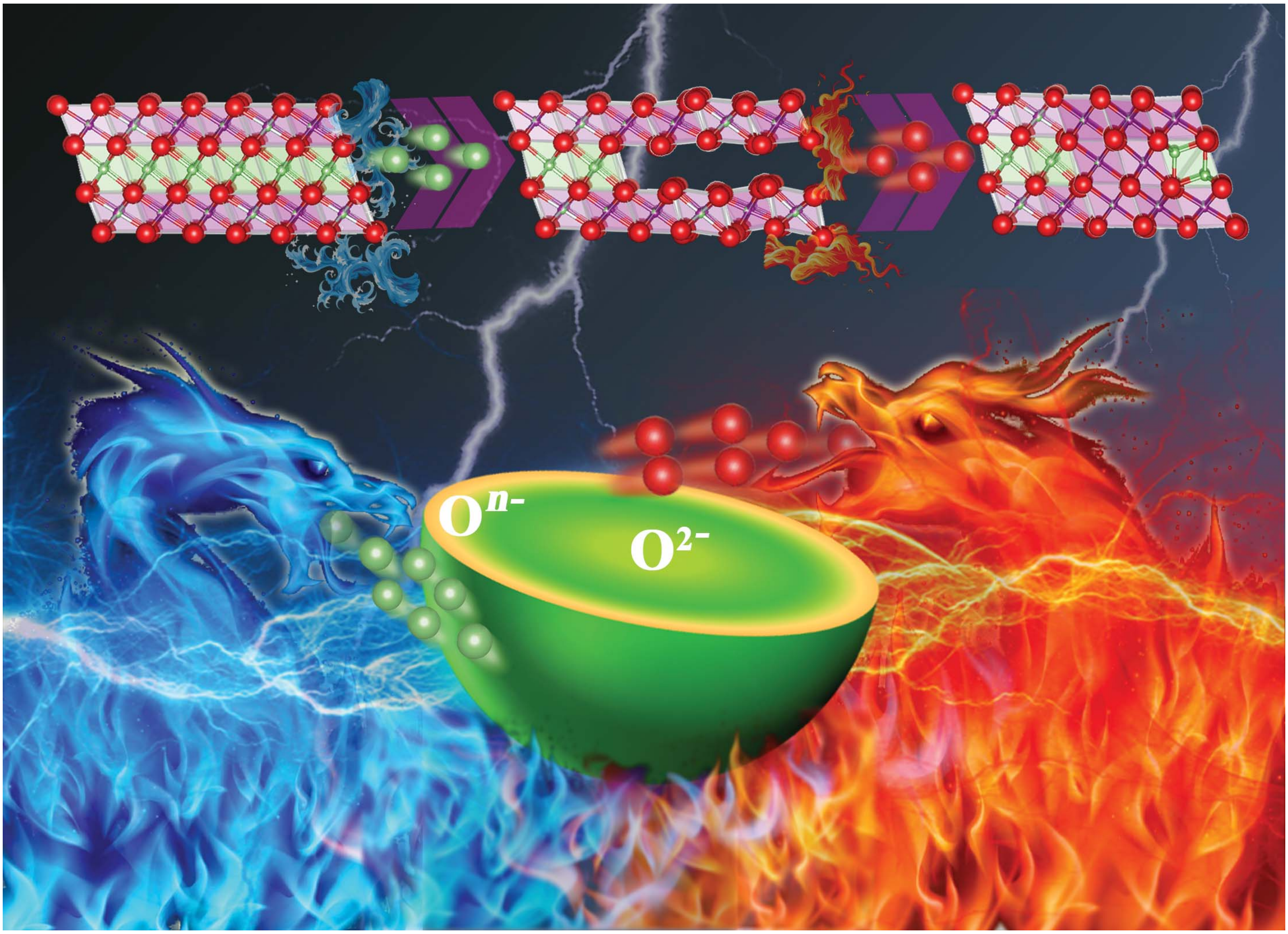

Highlighting a study on the peculiar role of surface oxygen anions in lithium- and manganese-rich layered oxides by a group of researchers led by Prof. Helmut Ehrenberg from Karlsruhe Institute of Technology.

Phosphoric acid and thermal treatments reveal the peculiar role of surface oxygen anions in lithium and manganese-rich layered oxides

Oxidized O^{n-} species ($0<n<2$) are formed on the surface of H_3PO_4-treated $Li[Li_{0.2}Ni_{0.2}Mn_{0.6}]O_2$ oxides (LLNMO), resulting from Li-ion deficiency and lattice distortion. Metastable O^{n-} could be easily released from the oxygen surface lattice forming O_2 *via* thermal treatment, accompanied by atomic rearrangement, surface reconstruction and layered-to-rock-salt/spinel transitions. The results demonstrate that the surface lattice structure plays a critical role in the electrochemical performance of LLNMO.

As featured in:

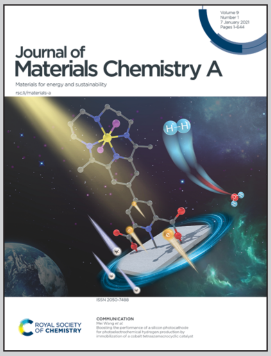

See Weibo Hua, Sylvio Indris, Julia Maibach *et al.*,
J. Mater. Chem. A, 2021, **9**, 264.

ROYAL SOCIETY
OF **CHEMISTRY**

rsc.li/materials-a

Journal of
Materials Chemistry A

PAPER

Cite this: *J. Mater. Chem. A*, 2021, **9**, 264

Phosphoric acid and thermal treatments reveal the peculiar role of surface oxygen anions in lithium and manganese-rich layered oxides†

Jiarong He,‡[a] Weibo Hua, ‡*[ab] Aleksandr Missiul, [c] Georgian Melinte,[de] Chittaranjan Das,[a] Akhil Tayal,[f] Thomas Bergfeldt,[a] Stefan Mangold,[g] Xinyang Liu,[a] Joachim R. Binder,[a] Michael Knapp,[a] Helmut Ehrenberg, [a] Sylvio Indris, *[a] Björn Schwarz [a] and Julia Maibach *[a]

The interplay between cationic and anionic redox activity during electrochemical cycling makes layered Li-rich oxides appealing cathodes for state-of-the-art lithium-ion batteries. However, it remains challenging as the origin of lattice oxygen activity is not yet fully understood. Here we report on the effects of a lithium-deficient layer in the near-surface region of Co-free Li-rich $Li[Li_{0.2}Ni_{0.2}Mn_{0.6}]O_2$ (LLNMO) achieved *via* a phosphoric acid surface treatment. Our results show that oxidized O^{n-} ($0 < n < 2$) species are formed on the surface of H_3PO_4-treated LLNMO resulting from Li ion deficiency and lattice distortion. The metastable O^{n-} could be easily released from the oxygen surface lattice forming O_2 *via* thermal treatment, accompanied by a surface reconstruction and a layered-to-rock-salt/spinel transition. The presented results demonstrate that the surface lattice structure plays a critical role in the electrochemical performance of LLNMO. This information provides new insights into the oxygen redox in LLNMO and opens up an opportunity for Li-rich cathodes to achieve long cycle life toward a broad range of applications in electrical energy storage devices.

Received 28th July 2020
Accepted 29th September 2020

DOI: 10.1039/d0ta07371g

rsc.li/materials-a

Introduction

Alkali-rich transition-metal (TM) oxide materials are of significant interest for advanced battery cathode materials, because they can create excess capacity beyond what is expected from the TM redox alone in stoichiometric cathode materials.[1–4] In comparison with the stoichiometric layered oxides (*i.e.* A[TM]O$_2$, square brackets indicate that the TM is on octahedral sites), some of the TM cations in the TM layer are replaced by alkali ions forming a superstructure ($A[A'_xTM_{1-x}]O_2$, $0 < x \le 1/3$).[5–7] It is currently believed that the extra capacity of these cathodes is derived from lattice oxygen redox, which is triggered by the initial charging process at high voltages (*e.g.* $\ge 4.5\ V_{Li^+/Li}$).[8–10] Among these compounds, Li- and Mn-rich layered oxides (LMLOs) are at the forefront of this area achieving high discharge capacities above 250 mA h g^{-1}.[11,12] However, the oxygen redox activity always causes changes in the crystallographic structure, surface inhomogeneity and release of lattice oxygen in LMLOs, thereby resulting in structural instability and severe voltage fading.[13,14]

Recently, extensive research efforts have been devoted to exploring the origin of the structural degradation of LMLOs upon high-voltage cycling. Several hypotheses have been proposed including layered-to-rock-salt/spinel phase transitions,[15,16] localization of oxygen electron holes[17] or formation of $Mn{-}\eta^1{-}O_2$ species,[18] TM over-oxidation,[19,20] irreversible O_2 loss with surface densification,[21,22] Li_2O removal with "MnO_2-like" phase formation,[23] generation of peroxo-like O_2^{m-} ($1 \le m \le 3$) dimers,[24,25] O-redox at the interface between the electrolyte and bulk,[26] *etc.* Generally, the commonly used carbonate-based electrolytes are not stable up to 5 V *versus* Li$^+$/Li, which causes interfacial side-reactions at the electrode surface forming

---

[a] Institute for Applied Materials (IAM), Karlsruhe Institute of Technology (KIT), Hermann-von-Helmholtz-Platz 1, 76344 Eggenstein-Leopoldshafen, Germany. E-mail: julia.maibach@kit.edu; sylvio.indris@kit.edu

[b] State Key Laboratory of Electronic Thin Films and Integrated Devices, University of Electronic Science and Technology of China, Chengdu, 610054, China. E-mail: weibo.hua@uestc.edu.cn

[c] CELLS-ALBA Synchrotron, Cerdanyola del Valles, E-08290 Barcelona, Spain

[d] Institute of Nanotechnology, Karlsruhe Institute of Technology (KIT), Hermann-von-Helmholtz-Platz 1, D-76344, Eggenstein-Leopoldshafen, Germany

[e] Helmholtz Institute Ulm (HIU) Electrochemical Energy Storage, Helmholtzstrasse 11, 89081 Ulm, Germany

[f] Deutsches Elektronen-Synchrotron DESY, Notkestrasse 85, D-22607 Hamburg, Germany

[g] Institute for Photon Science and Synchrotron Radiation, Karlsruhe Institute of Technology (KIT), Hermann-von-Helmholtz-Platz 1, D-76344 Eggenstein-Leopoldshafen, Germany

† Electronic supplementary information (ESI) available: Experimental section, Rietveld refinement results based on SRD data, crystallographic parameters, SEM-EDX images, XAS spectra and electrochemical performances of the samples. See DOI: 10.1039/d0ta07371g

‡ These authors contributed equally to this work.

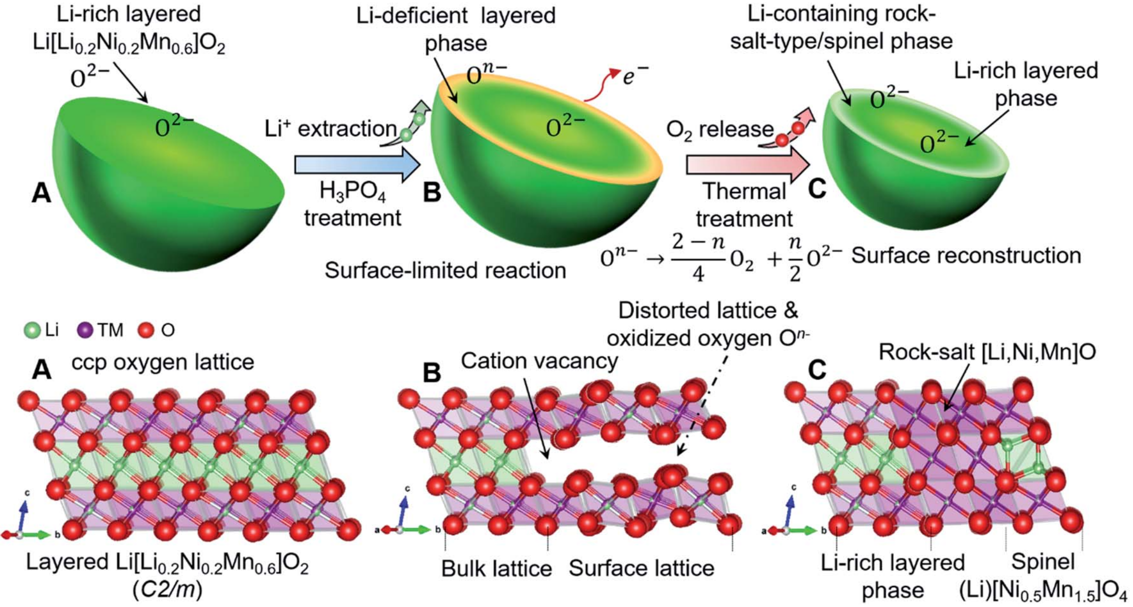

Scheme 1 Schematic illustration of chemically and thermally induced structural evolution of layered $Li[Li_{0.2}Ni_{0.2}Mn_{0.6}]O_2$ cathode materials, showing the formation of oxidized O^{n-} with surface lattice distortion and lithium deficiency *via* H_3PO_4 treatment, and the atomic rearrangement (phase transformation) with recrystallization after thermal treatment. (A) Pristine sample, (B) H_3PO_4-treated samples, (C) thermally treated sample.

a cathode–electrolyte interface (CEI) layer. Thereby, the degradation process of LMLOs is strongly influenced by the structure and reaction chemistry at the cathode surface.[27,28] Unfortunately, it is difficult to obtain precise chemical composition and real crystallographic information on the surface of LMLOs during electrochemical cycling.[29] Up to now, a clear picture of how the surface lattice oxide ions are oxidized, as lithium ions and electrons are extracted from the layered structure, has been missing.

Recently, chemically driven Li-ion extraction reaction has drawn widespread attention due to its fast reaction rate process. For example, Ramakrishnan *et al.* achieved an extended interfacial stability of Li-rich oxide cathodes on the surface through a strong H_2SO_4 acid rinsing, which could suppress the irreversible oxygen evolution and improve the cycling and rate performance.[8] Wu *et al.* tuned the oxygen redox reaction through the inductive effect with proton insertion in Li-rich oxides, thus stabilizing the oxygen activity during charging.[30] Paik *et al.* studied the acid leaching of the layered compound Li_2MnO_3, showing an H^+/Li^+ ion exchange with a shearing of the oxygen layers driven by hydrogen bonding, observed by ^6Li and ^2H MAS NMR measurements in conjunction with X-ray diffraction.[31] On the other hand, both Meng's group[12] and our group[32] found that the high voltage plateau at around 4.5 V of LMLOs in the first charging can be recovered by heating of the cycled electrode, suggesting that the high-voltage functionality of LMLOs is closely tied to their thermal stability. However, how the dilute phosphoric acid and thermal treatments affect the surface structure and chemistry of LMLOs is still unclear.

It is well known that the precipitation process is also one of the fastest reactions in aqueous solution.[33] Inspired by the production of a Li_3PO_4 precipitate,[34] we used low-concentration solutions of phosphoric acid to extract lithium ions from Co-free layered $Li[Li_{0.2}Ni_{0.2}Mn_{0.6}]O_2$ oxides (LLNMO) without obvious oxygen loss and H^+/Li^+ exchange. As determined by high-resolution synchrotron radiation diffraction (SRD), X-ray photoelectron spectroscopy (XPS) and transmission electron microscopy (TEM), the acid treatment leads to a considerably distorted surface lattice of LLNMO after the chemical extraction of lithium ions, which provides the prerequisites to form oxidized O^{n-} $(0 < n < 2)$ on the surface (see Scheme 1). To investigate the thermal stability of existing O^{n-} in the acid-treated samples, the materials were heated at high temperature. *In situ* high-temperature SRD (HTSRD) results reveal that the pristine LLNMO is stable during annealing, while a phase transition from a layered structure to a Li-containing rock-salt ($Fm\bar{3}m$) and/or a Li-containing spinel ($Fd\bar{3}m$) structure occurs in the H_3PO_4-treated materials after O_2 loss induced by the disproportionation of oxidized O^{n-} upon heating, which has never been reported before.

Results and discussion

The pure layered LLNMO (LLNMO-P) was prepared by a hydroxide co-precipitation method followed by a high-temperature lithiation reaction,[33,35] as evidenced by the SRD pattern in Fig. 1a. The acid-treated samples were obtained by homogeneously mixing LLNMO-P with different concentrations of H_3PO_4 solution (4% & 5%, mass ratio). The as-prepared materials were labelled as LLNMO-H4 and LLNMO-H5, respectively. All three samples were subsequently calcined at 900 °C for 2 hours in air to investigate the thermal stability of

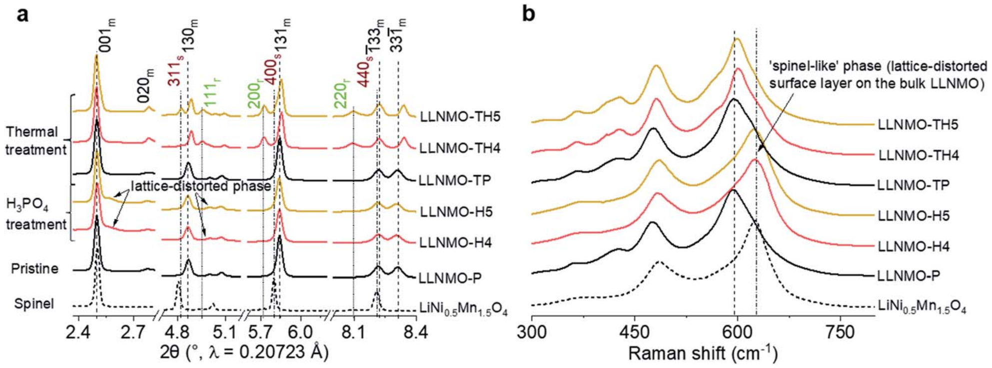

Fig. 1 Structural analysis of the prepared samples. (a) SRD patterns and (b) Raman spectra of the samples. In (a), m, r, and s stand for layered monoclinic phase (*C*2/*m*), rock-salt-type phase (*Fm*$\bar{3}$*m*), and spinel phase (*Fd*$\bar{3}$*m*). The 020_m reflection belonging to the honeycomb superstructure is visible for all products, demonstrating that the acid treatment and the thermal treatment do not affect the bulk monoclinic-layered structure (*C*2/*m*). In (b), the grey short dashed line indicates the peak position for the spinel $LiNi_{0.5}Mn_{1.5}O_4$ reference sample.

the oxides, which were marked as LLNMO-TP, LLNMO-TH4 and LLNMO-TH5, respectively. LLNMO-P treated with a high-concentration H_3PO_4 solution (15%; labelled as LLNMO-H15) and the typical high-voltage spinel $LiNi_{0.5}Mn_{1.5}O_4$ (LNMO) oxide were also prepared for comparison. An impurity phase $TMPO_4$ (TM = Ni, Mn) is found in LLNMO-H15, see ESI Fig. S2g,† suggesting that LLNMO-P would dissolve in high-concentration phosphoric acid. In this work, we focus on the low-concentration H_3PO_4 treatment. Details of the preparation process are presented in the ESI.†

Compared to the SRD pattern of LLNMO-P, there is almost no shift in the main reflections in the SRD patterns for both LLNMO-H4 and LLNMO-H5. The Ni and Mn oxidation states for the acid-treated materials do not change noticeably, and remain at +2 and +4, respectively, as determined by hard X-ray absorption spectroscopy (XAS, see ESI Fig. S1†). These results demonstrate that the acid treatment does not cause obvious changes in the electronic structure of the bulk oxides. Surprisingly, several additional weak reflections close to the main layered phase appear in the SRD patterns of LLNMO-H4 and LLNMO-H5, *e.g.* a broad reflection at ∼2.5° on the right side of the 001_m reflection. These Bragg reflections are always observed for the LMLOs when they are charged to potentials >4.5 V, proposed to be related to a spinel-like (*Fd*$\bar{3}$*m*) phase on the surface (see the spinel LNMO reference)[36]. Normally, the 001_m reflection of layered LLNMO shifts toward lower scattering angles firstly during charging, and then moves to higher 2-theta angles with further Li-ion extraction, corresponding to an initially increased lattice parameter *c* caused by increasing electrostatic repulsion and later to a contraction of the *c*-axis resulting from oxygen oxidation or TM migration.[37,38] Therefore, the broad reflection on the right side of the 001_m reflection can be ascribed to the over-delithiated surface layer on LLNMO after the H_3PO_4 treatment. Raman spectra were additionally recorded to further trace the structural changes after the acid treatment (Fig. 1b). The main peak observed for the H_3PO_4-treated materials, *i.e.* LLNMO-H4 and LLNMO-H5, shifts from 598 to 630 cm^{-1} with respect to the LLNMO-P, manifesting the changes in the A_{1g} vibration of the Raman-active mode from a layered to a spinel LNMO phase.[39,40] This is regarded as a complementary indicator of spinel-like phase formation on the surface. However, the fundamental question, which naturally arises, is "What is the nature of this often-observed spinel-like (*Fd*$\bar{3}$*m*) phase?"

XPS analyses were carried out to investigate the surface composition and oxidation states of the elements in the specimens (see Fig. 2 and ESI Fig. S3†). In Fig. 2, the peak found at around 52.9 eV can be assigned to the lattice Li^+ (Fig. 2a) and the major peaks at 529.6 eV can be ascribed to the lattice oxide ions O^{2-}, while the weak components at higher binding energies (531.9 eV and 533.1 eV) in the O 1s core level spectrum

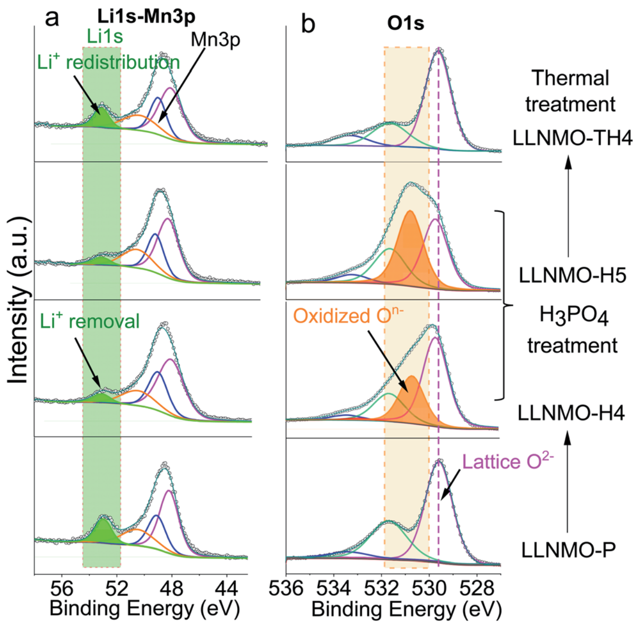

Fig. 2 Li 1s (a) and O 1s (b) XP spectra of the pristine and acid treated samples, showing the formation of oxidized O^{n-} on the surface of the crystallites with the extraction reaction of lithium ions *via* the H_3PO_4 treatment (LLNMO-H4 and LLNMO-H5) and the decomposition of oxidized O^{n-} with lithium ion redistribution after thermal treatment (LLNMO-TH4).

correspond to surface bound species, for example oxygen in carbonates and hydroxides (Fig. 2b). After the acid treatment, the relative intensity of the Li peak at 52.9 eV decreased substantially in the Li 1s spectrum of LLNMO-H4 and LLNMO-H5, indicating that Li ions are extracted from the surface lattice of crystallites. Simultaneously, a peak at ~530.6 eV appears in the O 1s region which is characteristic of the formation of oxidized O^{n-} in the surface lattice of the acid-treated LLNMO samples.[25] All samples showed very similar peak shapes and binding energy (BE) positions for Ni $2p_{3/2}$, Mn $3p_{3/2}$ and Mn 3s (ESI Fig. S3†), indicating that the transition metal oxidation states were the same irrespective of the sample treatment. A multiplet splitting method was adopted to evaluate the oxidation states of Ni and Mn in detail, as demonstrated by Biesinger[41] and Azmi *et al.*[42] The fitting results indicate that for all samples the transition metals are present in surface oxidation states of Ni^{2+} and Mn^{4+}, respectively. The Mn oxidation state is further confirmed in the Mn 3s spectrum as a distinctive satellite appears at 4.5 eV higher binding energy compared to the main Mn 3s peak.

To investigate the morphological differences of LLNMO-P and the acid-treated samples, scanning electron microscopy (SEM) was carried out. As shown in Fig. 3a, the LLNMO-P particles are agglomerates consisting of several fine platelet-like crystallites, with a primary crystal size of around 100–500 nm. Fig. 3d displays a high-resolution TEM (HRTEM) image of LLNMO-P along the *c*-axis. The measured interplanar spacing is approximately 4.75 Å, corresponding to the planar distance between adjacent TM layers of layered LLNMO, *i.e.* the $(001)_m$ plane. Although the crystal morphology and the bulk lattice remain basically unchanged after the H_3PO_4 treatment (see Fig. 3b and e, and S4†), a severe lattice distortion at the surface is clearly observed for the LLNMO-H5 in the HRTEM image. The distortion results from Li ions being removed from the surface lattice, leaving Li-site cation vacancy defects. The distorted lattice can elongate or shorten the distance between two adjacent oxygen ions (O^{2-}). The former might result from an increased electrostatic repulsive force within the cubic-close packed (ccp) oxygen lattice, while the latter effect might be attributed to the formation of molecular O_2 inside the solid[18] or localized electron holes on oxygen[17] or peroxo oxygen dimers.[43]

ESI Fig. S2† shows the results of the Rietveld refinement against the SRD patterns for the samples presented in Fig. 1. Although in the SRD it is difficult to distinguish between layered and spinel phases on the surface from a nano-scale with the corresponding broadening of reflections,[38] HRTEM images show that no TM cations are pronouncedly observed in the Li layer of acid-treated samples (see the HRTEM images above). This suggests that a potential cubic spinel phase (AB_2O_4, $Fd\bar{3}m$) as indicated by Raman can actually be excluded since for spinel a quasi-equal distribution of TM is characteristic. Therefore, Rietveld refinements were performed assuming a multiple phase model, *i.e.* a monoclinic layered $Li[Li_{0.2}Ni_{0.2}Mn_{0.6}]O_2$ ($C2/m$) and a defective layered $Li_{1-x}[TM]O_2$ ($R\bar{3}m$), which seems more appropriate to account for the surface phase than a spinel phase, in LLNMO-H4 and LLNMO-H5. The weight fraction of the Li-defective layered phase is ~6% for LLNMO-H4, and ~8% for LLNMO-H5, respectively. Chemical compositions were investigated by inductively coupled plasma optical emission spectroscopy (ICP-OES). ICP-OES results suggest that the atomic ratio of Ni : Mn in the three samples is very close to the theoretical value (1 : 3, see Table 1). The lithium concentrations in the H_3PO_4-treated samples decrease significantly, which provides convincing evidence for the chemical extraction of

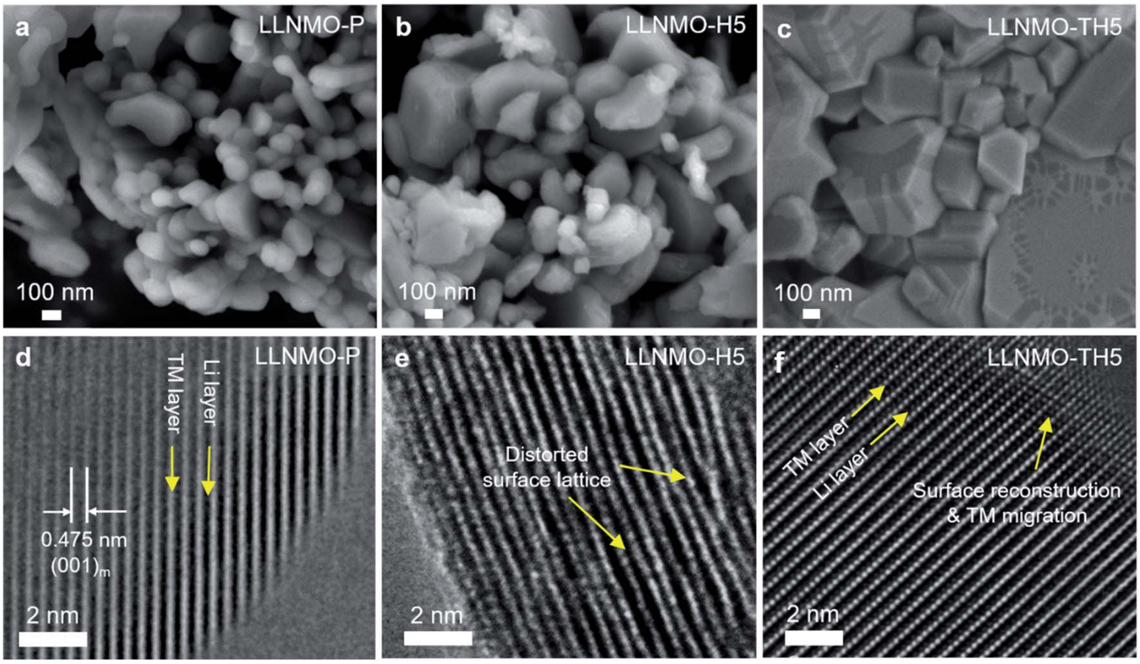

Fig. 3 SEM and HRTEM images of (a and d) LLNMO-P, (b and e) LLNMO-H5 and (c and f) LLNMO-TH5.

Table 1 Chemical analysis results of selected samples[a]

	Molar ratio				
Samples	Li	Ni	Mn	O	P
LLNMO-P	1.21 ± 0.03	0.20 ± 0.01	0.61 ± 0.01	2.28 ± 0.18	—
LLNMO-H4	1.07 ± 0.03	0.20 ± 0.01	0.62 ± 0.01	2.19 ± 0.18	0.01 ± 0.001
LLNMO-H5	1.04 ± 0.03	0.20 ± 0.01	0.63 ± 0.01	2.23 ± 0.18	0.02 ± 0.002
LLNMO-TP	1.24 ± 0.03	0.20 ± 0.01	0.61 ± 0.01	2.24 ± 0.18	—
LLNMO-TH4	1.07 ± 0.03	0.20 ± 0.01	0.62 ± 0.01	2.17 ± 0.18	0.01 ± 0.001
LLNMO-TH5	1.04 ± 0.03	0.20 ± 0.01	0.63 ± 0.01	2.17 ± 0.18	0.02 ± 0.002

[a] Note: determining whether or not oxygen loss occurred through acid treatment could not be deduced from this table because of the larger experimental error in the case of oxygen.

lithium ions from the crystal structure of Li-rich layered oxides during the acid treatment. Therefore, the so-called "spinel-like" phase formed on the surface is most likely a lithium-deficient layered phase with a lattice distortion. Additionally, bubbles are visible during the phosphoric acid treatment. Based on these results, a reduction–oxidation reaction is proposed:

$$\begin{aligned}&Li_{1.2}{Ni_{0.2}}^{2+}{Mn_{0.6}}^{4+}{O_2}^{2-}\\&\quad+\frac{x}{3}H_3PO_4 \rightarrow Li_{1.2-x}{Ni_{0.2}}^{2+}{Mn_{0.6}}^{4+}{O_2}^{(2-0.5x)^-}+\frac{x}{3}Li_3PO_4\downarrow\\&\quad+\frac{x}{2}H_2\uparrow(0<x<0.2)\end{aligned} \tag{1}$$

In order to gain further insights into the metastable O^{n-} on the surface of the Li- and Mn-rich layered oxides, thermal treatment was used and the samples were analysed by SRD and Raman spectroscopy. The reflections in the SRD pattern of LLNMO-TP do not change considerably, as evidenced by comparison with LLNMO-P (see Fig. 1a), revealing a good structural and chemical stability of the prepared $Li[Li_{0.2}Ni_{0.2}Mn_{0.6}]O_2$. In contrast, for the acid-treated samples, in addition to the main monoclinic layered phase ($C2/m$), a set of reflections, *i.e.* 111_r, 200_r and 220_r, indexed to the Li-containing rock-salt-type phase ($Fm\bar{3}m$), is clearly observed in the SRD pattern of the thermally treated LLNMO-TH4. LLNMO-TH5 is found to be a mixture of a Li-rich layered phase ($C2/m$), a Li-containing rock-salt-type phase ($Fm\bar{3}m$) and a Li-containing spinel phase ($Fd\bar{3}m$), and their weight fractions are 73(2), 13(2) and 14(2)% (see ESI Fig. S2 and Table S1†). Thermodynamically, as lithium and oxygen are successively released from the surface lattice, the Li-rich $Li[Li_{0.2}Ni_{0.2}Mn_{0.6}]O_2$ oxide tends to transform into a Li-containing rock-salt-type phase ($Fm\bar{3}m$) and then into a Li-containing spinel phase ($Fd\bar{3}m$), which matches precisely with reported results.[7] These phase changes again offer compelling evidence for a continuous lithium extraction during the H_3PO_4 treatment. Interestingly, some reflections in the SRD patterns of LLNMO-TH4 and LLNMO-TH5 (*e.g.* 001_m and $\bar{1}33_m$) remain at the same diffraction angles (2θ) compared to the SRD patterns of the LLNMO-P, while other reflections such as 130_m, 131_m and $33\bar{1}_m$ shift toward higher scattering angles. All of this indicates that the average TM–TM inter-slab distance of the monoclinic layered structure (indicative of Li content and c lattice parameter) remains the same after the thermal treatment, but the average TM–TM intra-slab distance of the layered structure becomes smaller (*i.e.* a and b lattice parameters, see ESI Table S1†). Furthermore, the SRD analysis implies that the cubic rock-salt/spinel phases with a coherent ccp oxygen lattice formed on the surface could compress the a–b plane in the interior of the layered crystal and cause surface reconstruction (see the SEM images in Fig. 3c).

After the thermal treatment, the main peak at ~630 cm^{-1} in the Raman spectra observed for the acid treated LLNMO-H4 and LLNMO-H5 moves to 603 cm^{-1} for LLNMO-TH4 and LLNMO-TH5 (Fig. 1b). It seems that the "spinel-like" phase in LLNMO-H4 and LLNMO-H5 transforms back to the Li-rich layered phase. Indeed, the first interpretation of the Raman spectra after acid treatment indicating a cubic "spinel-like" structure is meagre and not straightforward because no real spinel phase (AB_2O_4) is formed in the acid-treated samples but rather a lithium-deficient layered phase with a lattice distortion and an O3 structure (ABCABC oxygen stacking sequence, see the discussion above). The results are similar to those reported previously by Yin *et al.*[44] and interpreted by them as the formation of a densified layered phase with the O3 $R\bar{3}m$ structure. In the XP spectra of LLNMO-TH4 (Fig. 2), the oxygen peak at ~530.6 eV disappears, signifying the disintegration of oxidized O^{n-} on the surface during thermal treatment (*i.e.* $O^{n-}\xrightarrow{\Delta}\frac{2-n}{4}O_2+\frac{n}{2}O^{2-}$, Δ indicates heating). It is well known that the oxygen anions offer metal coordination sites in the layered structure.[11,45] The oxygen release is therefore supposed to be accompanied by surface atomic rearrangement. The intensity of the Li 1s peak in the XP spectra of LLNMO-TH4 increases, compared to that of LLNMO-H4, pointing towards Li ions from the bulk structure migrating into the empty octahedral/tetrahedral sites on the surface during annealing (*i.e.* lithium redistribution). Moreover, a step and terrace texture is found to form on the surface of LLNMO-TH5, see Fig. 3c, illustrating the surface reconstruction and the recrystallization during the thermal treatment of LLNMO-H5 (see also the SEM-Energy Dispersive X-ray Analysis (EDX) images of selected samples in ESI Fig. S5–S8†). The TEM image of LLNMO-TH5 (Fig. 3f) shows a significant amount of TM migration from the TM layer to the Li layer on the surface that promotes the formation of the cubic spinel/rock-salt structure, which is supposed to accommodate a certain amount of Li ions, as evidenced by the XPS results in Fig. 2.

In order to trace the chemical and structural evolution of the acid-treated samples with surface defects, thermogravimetric (TG) and *in situ* high-temperature synchrotron radiation diffraction (HTSRD) measurements were carried out, as shown in Fig. 4 and ESI Fig. S9–S12.† TG curves show that there are two weight loss stages for both LLNMO-H4 and LLNMO-H5 in air up to 900 °C, as compared to an almost constant weight for LLNMO-P during the heating and cooling processes (Fig. 4a). The first weight loss at about 300 °C is attributed to the decomposition of surface oxidized O^{n-} into O_2; the second weight loss between 700 and 900 °C is most likely due to the release of surface and/or bulk lattice oxygen ions (*i.e.* $2O^{2-} \xrightarrow{\Delta} O_2 + 4e^-$). Importantly, a weight gain (*i.e.* oxygen uptake) occurs for the H_3PO_4-treated oxides during cooling, leading to an overall weight loss of ~2% for LLNMO-H4 and ~3% for LLNMO-H5, respectively, after thermal treatment (heating and cooling). These results match with the theoretical values, *e.g.* $Li_{1.04}Ni_{0.2}Mn_{0.6}O_2 \xrightarrow{\Delta} Li_{1.04}Ni_{0.2}Mn_{0.6}O_{1.92} + 0.04\ O_2\uparrow$, revealing that lattice oxygen is not released from the crystal structure extensively during H_3PO_4 treatment. Note that the Ni and Mn valence states on the surface remain almost constant (Ni^{2+} and Mn^{4+}) after the H_3PO_4 and thermal treatment (see ESI Fig. S3†), while the amount of lithium ions on the surface is increased in the acid-treated sample after heating (see Fig. 2a). Therefore, the weight gain during cooling reveals that Li ions are gradually redistributed across the entire crystal structure, which causes oxygen incorporation to maintain electroneutrality and provide more coordination sites for the migrated Li ions forming a Li-containing rock-salt/spinel structure on the surface (see the discussion below). Oxygen loss and oxygen uptake at high temperatures >700 °C are consistent with the reversible changes in the lattice parameters of the layered phase during heating and cooling (see ESI Fig. S12†). However, the lattice parameters of LLNMO-H4 and LLNMO-H5 do not return to the initial value after thermal treatment when compared with LLNMO-P, which indicates the destabilization of the bulk material.

In the SRD patterns acquired during continuous heating, all reflections of LLNMO-P move to lower two-theta angles (see Fig. 4b). During cooling, all reflections tend to shift towards their initial position. The difference in lattice parameters a, b, c, and V of LLNMO-P before and after heating is 0.0044(5) Å, 0.0067(5) Å, 0.0039(5) Å, and 0.4772(5) $Å^3$, respectively, again proving the excellent thermal stability of LLNMO-P. Heating of the H_3PO_4-treated samples up to 300 °C causes the weak broad reflection at around 10°, which corresponds to the Li-deficient layered phase and overlaps with the $002_m/\bar{1}12_m$ reflections belonging to the monoclinic layered phase, to vanish, see Fig. 4c and d, in good agreement with the oxygen loss observed in the TG curves. No new reflections in the *in situ* HTSRD patterns of LLNMO-H4 and LLNMO-H5 appear until the temperature is increased to ~700 °C, implying that a certain amount of lithium and oxygen vacancies on the surface does not lead to an immediate phase transition in the Li-rich layered oxides (kinetic control). With a further increase of temperature to 900 °C, the 111_r reflection of a disordered Li-containing rock-salt structure ($Fm\bar{3}m$) becomes sharp in both LLNMO-H4 and LLNMO-H5,

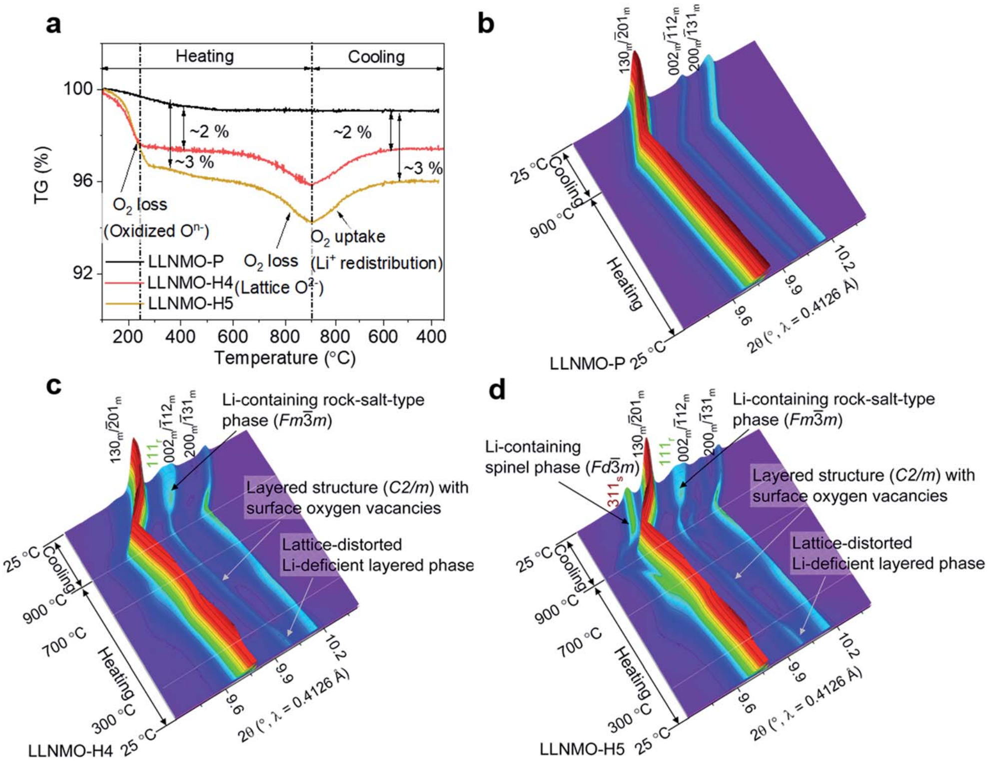

Fig. 4 (a) TG curves of the samples, and *in situ* HTSRD patterns of (b) LLNMO-P, (c) LLNMO-H4 and (d) LLNMO-H5.

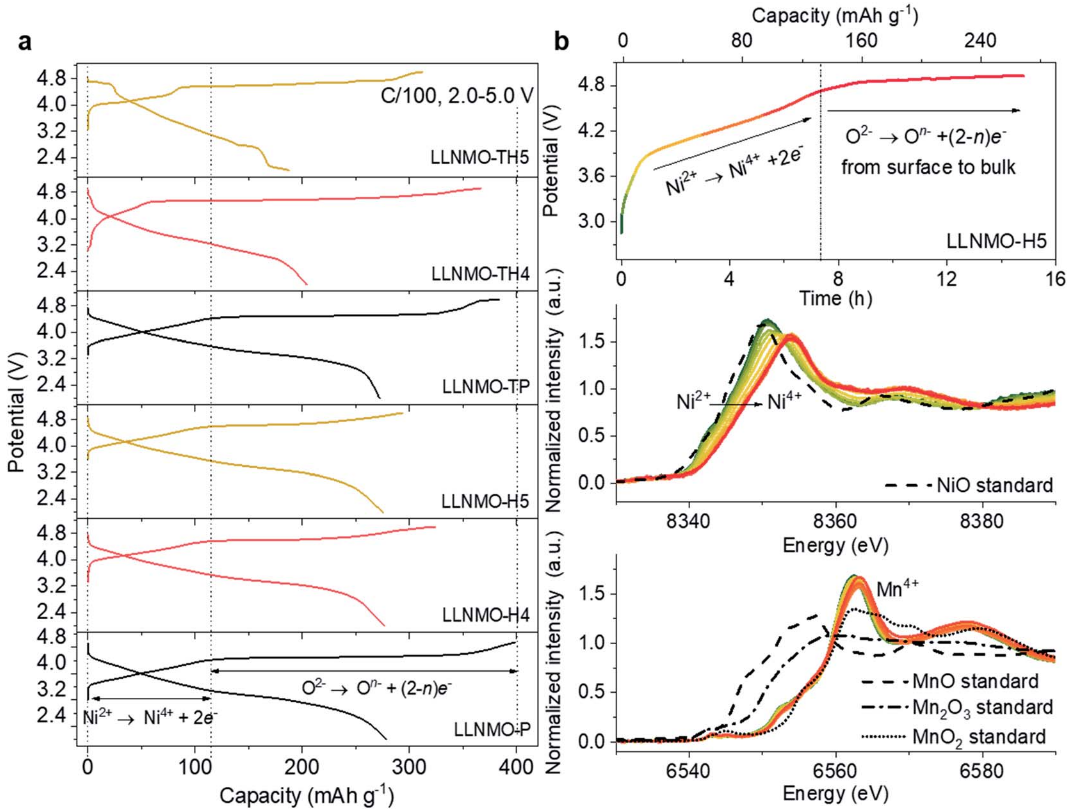

Fig. 5 (a) The initial capacity *versus* voltage profiles of the electrodes at a C-rate of 0.01C; (b) *in situ* XANES spectra at Ni and Mn K-edges of the LLNMO-H5 electrode during the first charging process.

while a large shift in the 311_s reflection corresponding to the Li-containing spinel structure ($Fd\bar{3}m$) is clearly found in LLNMO-H5. The structural changes are probably related to the defects, more specifically oxygen vacancies, generated on the surface of acid-treated oxides at high temperature (see Fig. 4a). These could effectively contribute to the ionic migration and thus result in the phase transformation from a "Li/O-poor" defective layered structure to a Li-containing cubic rock-salt/spinel structure.[45] The increasing intensity of the new reflections during cooling indicates that the oxygen anions are incorporated into the surface lattice to create more coordination sites for TM/Li cations (higher content of Li-containing cubic rock-salt-type/spinel phases, see ESI Table S3†). These results also suggest that the thermal treatment does not affect the lithium content of the oxides noticeably according to the $Li_xNi_{0.2}Mn_{0.6}O_y$ oxide phase diagram.[7] Finally, the formed Li-containing rock-salt/spinel structures are maintained after cooling to room temperature. Therefore, the overall reaction during the thermal treatment can be described as follows:

$$Li_{1.2-x}Ni_{0.2}{}^{2+}Mn_{0.6}{}^{4+}O_2{}^{(2-0.5x)-} \xrightarrow{\Delta} Li_{1.2-x}Ni_{0.2}{}^{2+}Mn_{0.6}{}^{4+}O_{2-0.5x}{}^{2-} + \frac{x}{2}O_2\uparrow \quad (2)$$

To evaluate the relation between the defect structure and electrochemical properties, electrochemical characterization experiments were performed using CR2032-type coin cells at room temperature. A low current density of 0.01C (1C = 320 mA g^{-1}) and a wide voltage range (2.0–5.0 V) were firstly used to minimize polarization in the charging process and to ensure a fully charged state, as displayed in Fig. 5a and ESI S13.† The initial charge curves of all electrodes show a comparably monotonic region below 4.5 V and a voltage plateau at approximately 4.6 V *vs.* Li^+/Li. Except for the cathodes based on LLNMO-TH4 and LLNMO-TH5, the cathodes exhibit a specific capacity of ~120 mA h g^{-1} at voltages <4.5 V, which corresponds to the extraction of 0.4 Li ion from $Li[Li_{0.2}Ni_{0.2}Mn_{0.6}]O_2$ and the oxidation of nickel(II) ions (*i.e.* $0.2Ni^{2+} \rightarrow 0.2Ni^{4+} + 0.4e^-$).[46] The lower capacity of LLNMO-TH4 and LLNMO-TH5 cathodes in this region could be due to the migration of some Ni^{2+} cations into the octahedral sites in the rock-salt structure and/or the tetrahedral sites in the spinel structure. The two plateaus at about 4.7 V found in the LLNMO-TH5 cathode (see Fig. 5a and ESI Fig. S13f†) are the characteristics of the spinel $LiNi_{0.5}Mn_{1.5}O_4$ structure. The presence of these plateaus is thus in good agreement with the SRD analysis, which also indicates a spinel structure for LLNMO-TH5. Noticeably, the acid-treated electrodes, LLNMO-H4 and LLNMO-H5, show almost the same capacity as that of LLNMO-P in the low-voltage region (<4.5 V). This provides evidence that the TM cations, at least Ni ions, are not oxidized during the acid treatment. *In situ* X-ray absorption near-edge structure (XANES) experiments were carried out to investigate the charge compensation mechanism in LLNMO-H5 (see Fig. 5b). There is no significant change in the Mn K-edge spectra of LLNMO-H5 during charging, and all spectra can

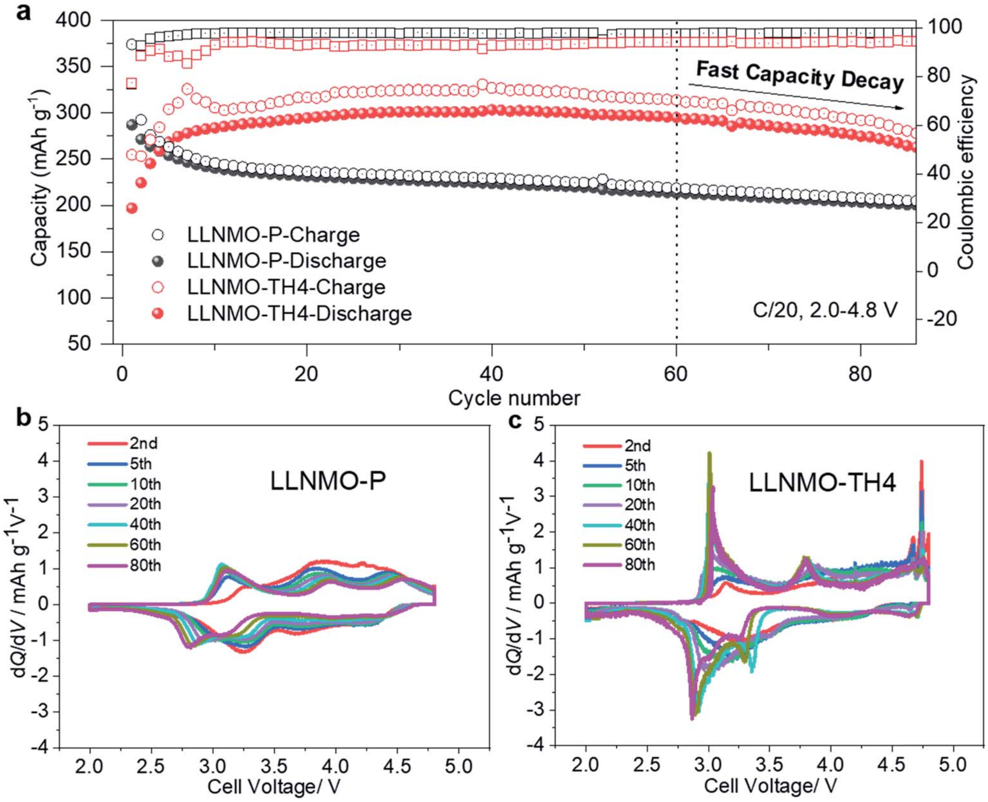

Fig. 6 (a) Cycling performance of the LLNMO-P and LLNMO-TH4 electrodes between 2.0 and 4.8 V at 0.05C; d*Q*/d*V* plots of (b) LLNMO-P and (c) LLNMO-TH4 samples at different cycles. A pair of sharp peaks at about 4.7 V in the d*Q*/d*V* curves of LLNMO-TH4 suggests the presence of a high-voltage spinel phase $LiNi_{0.5}Mn_{1.5}O_4$.

be assigned to Mn^{4+}. The Ni K absorption edge shifts towards higher energy as the voltage increases to 4.5 V, suggesting electron removal from the Ni^{2+} ions ($Ni^{2+} \rightarrow Ni^{4+} + 2e^-$). After charging to voltages higher than 4.6 V, no further changes in the XANES spectra are observed, indicating that the nickel valence state does not change considerably. Thus, the extra capacity of LLNMO-H5 (~180 mA h g^{-1}), originating from the long plateau at 4.6 V, can be ascribed to lattice oxide ion oxidation. The first charge capacity of LLNMO-H4 and LLNMO-H5 with an oxidized oxide surface layer is 324.3 and 293.6 mA h g^{-1}, respectively, which is lower than that of LLNMO-P (398.9 mA h g^{-1}). Except for LLNMO-TH4 and LLNMO-TH5 (self-formation of a Li-containing rock-salt/spinel surface layer), the electrodes exhibit a comparable initial discharge capacity, *i.e.* 278(3) mA h g^{-1}. Taken together, electrochemically driven oxide oxidation is supposed to participate in the de-lithiation reaction at high voltages (>4.5 V) and start from the surface lattice (a large amount of cation vacancies).

From a practical application perspective, the fabricated cells were galvanostatically cycled within the narrow voltage range of 2.0–4.8 V at 0.05C. The initial charge–discharge voltage profiles of the electrodes are shown in ESI Fig. S14.† A large overpotential on charging can be observed in the acid-treated electrodes, as supported by an increased charge transfer resistance in the electrochemical impedance spectroscopy (EIS) measurements shown in ESI Fig. S15 and Table S4.† The high polarization is attributed to the oxidized O^{n-} surface layer with lattice distortion, which could lead to a high diffusion barrier for Li ions, and thus results in a lower capacity and a shorter plateau at 4.6 V. Previous studies have suggested that the electrochemical performance of the electrodes can be effectively improved by modulating the Li/Ni disorder in layered cathode materials.[47–50] After surface reconstruction from a layered to a Li-containing disordered rock-salt structure *via* thermal treatment, the LLNMO-TH4 electrode exhibits outstanding cycling performance, as shown in Fig. 6a. Even if the coulombic efficiency of LLNMO-TH4 is only around 93% during cycling, a high capacity of 297.2 mA h g^{-1} can be achieved after 60 cycles, which is much higher than that of LLNMO-P (213.0 mA h g^{-1}). The low coulombic efficiency of LLNMO-TH4 is probably due to the Li-containing rock-salt phase on the surface that acts as a diffusion barrier layer for Li ion transport, which results in a dramatic capacity decrease after 60 cycles (see Fig. 6a). The corresponding derivative capacity–voltage (d*Q*/d*V*) plots for the two electrodes at various cycles are shown in Fig. 6b and c. A peak at around 3 V corresponding to the $Mn^{3+/4+}$ redox activity emerges in both electrodes upon cycling, especially for the LLNMO-TH4 electrode, suggesting that the capacity originating from the bulk lattice oxygen redox activity is reduced to some extent.

Conclusion

In summary, a simple and reproducible method, *i.e.* H_3PO_4 treatment, is proposed for chemical de-intercalation of lithium ions from Li- and Mn-rich layered oxides. Lattice distortion and oxidized O^{n-} at the surface of the acid-treated Li-rich oxides are observed. The Li-deficient surface layer, *i.e.* a defective layered phase with lattice distortion, produces the structural features of a spinel-like phase in the SRD patterns and Raman spectra. Significant structural changes occur on the defective surface during heating and cooling processes. With the release of oxygen, the Li/O-deficient layered structure on the surface of the Li-rich oxides tends to transform into a Li-containing cubic rock-salt/spinel structure, concomitant with atomic rearrangement, surface reconstruction and Li redistribution. These results further demonstrate that the electrochemical properties are closely tied to the surface structure of the Li-rich cathode materials. Surface lattice distortion can block the lithium diffusion channels, while the coherent oxygen lattice with moderate Li/TM cation disorder on the surface after acid and thermal treatment is beneficial for improving the cycling performance of LLNMO cathodes. The knowledge gained from this work on acid and heat surface treatment could help to further improve the cycle life of high-energy Li-rich oxides for Li ion batteries and other electrode materials for post-lithium ion batteries.

Author contributions

J. H., W. H., and J. M. oversaw the project; J. H. and W. H. carried out sample preparation and experimental work, and discussed with M. K., J. M., J. R. B., H. E., S. I. and B. S; J. H. W. H., A. M., A. T., S. M., and S. I. performed the synchrotron diffraction measurements; the data were analysed by J. H., W. H., C. D., X. L., J. M., T. B., and S. I.; W. H. wrote the preliminary draft with input from J. H. and J. M.; all authors contributed to interpreting the findings, and reviewing and revising the manuscript.

Conflicts of interest

The authors declare no competing financial interest.

Acknowledgements

J. H. received financial support from the Sino-German (CSC-DAAD) Postdoc Scholarship Program, 2018 (201800260016). W. H. received financial support from the China Scholarship Council (CSC) and the Helmholtz-OCPC Postdoc-Program. We acknowledge DESY (Hamburg, Germany), a member of the Helmholtz Association HGF, for the provision of experimental facilities. We gratefully acknowledge Alexander Schökel and Martin Etter at beamline P02.1 at PETRA-III for the synchrotron-based diffraction experiments, and Wolfgang Caliebe and Vadim Murzin at beamline P64 at PETRA-III for the XAS measurements. Some of these experiments were performed at the MSPD beamline at ALBA Synchrotron with the collaboration of ALBA staff. The XPS, TEM and BTA characterization experiments were performed at the Karlsruhe Nano Micro Facility (KNMF), a Helmholtz research infrastructure operated at KIT. The authors thank Christina Odemer for help with the TG/DSC measurements, Udo Geckle (IAM-ESS, KIT) for help with the SEM experiments, Liuda Mereacre (IAM-ESS, KIT) for help with the Raman measurements and Raheleh Azmi (IAM-ESS, KIT) for the XPS discussion about the Ni/Mn multiplet fitting. This work contributes to the research performed at CELEST (Center for Electrochemical Energy Storage Ulm-Karlsruhe).

References

1 M. Ben Yahia, J. Vergnet, M. Saubanère and M.-L. Doublet, *Nat. Mater.*, 2019, **18**, 496–502.

2 G. Van Tendeloo, E. J. Berg, J.-M. Tarascon, A. M. Abakumov, D. Foix, P. Novak, G. Rousse, R. Dominko, D. Gonbeau, M.-L. Doublet, M. Saubanere and E. McCalla, *Science*, 2015, **350**, 1516–1521.

3 J. Lee, D. A. Kitchaev, D.-H. Kwon, C.-W. Lee, J. K. Papp, Y.-S. Liu, Z. Lun, R. J. Clément, T. Shi, B. D. McCloskey, J. Guo, M. Balasubramanian and G. Ceder, *Nature*, 2018, **556**, 185–190.

4 Y. Liang, C. Zhao, H. Yuan, Y. Chen, W. Zhang, J. Huang, D. Yu, Y. Liu, M. Titirici, Y. Chueh, H. Yu and Q. Zhang, *InfoMat*, 2019, **1**, 6–32.

5 X. Rong, J. Liu, E. Hu, Y. Liu, Y. Wang, J. Wu, X. Yu, K. Page, Y. S. Hu, W. Yang, H. Li, X. Q. Yang, L. Chen and X. Huang, *Joule*, 2018, **2**, 125–140.

6 Y. Qiao, S. Guo, K. Zhu, P. Liu, X. Li, K. Jiang, C. J. Sun, M. Chen and H. Zhou, *Energy Environ. Sci.*, 2018, **11**, 299–305.

7 W. Hua, S. Wang, M. Knapp, S. J. Leake, A. Senyshyn, M. Yavuz, J. R. Binder, C. P. Grey, H. Ehrenberg, S. Indris and B. Schwarz, *Nat. Commun.*, 2019, **10**, 5365.

8 S. Ramakrishnan, B. Park, J. Wu, W. Yang and B. D. McCloskey, *J. Am. Chem. Soc.*, 2020, **142**, 8522–8531.

9 Z. W. Lebens-Higgins, H. Chung, M. J. Zuba, J. Rana, Y. Li, N. V. Faenza, N. Pereira, B. D. McCloskey, F. Rodolakis, W. Yang, M. S. Whittingham, G. G. Amatucci, Y. S. Meng, T. L. Lee and L. F. J. Piper, *J. Phys. Chem. Lett.*, 2020, **11**, 2106–2112.

10 E. Hu, X. Yu, R. Lin, X. Bi, J. Lu, S. Bak, K.-W. Nam, H. L. Xin, C. Jaye, D. A. Fischer, K. Amine and X.-Q. Yang, *Nat. Energy*, 2018, **3**, 690–698.

11 W. Hua, M. Chen, B. Schwarz, M. Knapp, M. Bruns, J. Barthel, X. Yang, F. Sigel, R. Azmi, A. Senyshyn, A. Missiul, L. Simonelli, M. Etter, S. Wang, X. Mu, A. Fiedler, J. R. Binder, X. Guo, S. Chou, B. Zhong, S. Indris and H. Ehrenberg, *Adv. Energy Mater.*, 2019, **8**, 1803094.

12 A. Singer, M. Zhang, S. Hy, D. Cela, C. Fang, T. A. Wynn, B. Qiu, Y. Xia, Z. Liu, A. Ulvestad, N. Hua, J. Wingert, H. Liu, M. Sprung, A. V. Zozulya, E. Maxey, R. Harder, Y. S. Meng and O. G. Shpyrko, *Nat. Energy*, 2018, **3**, 641–647.

13 D. Seo, J. Lee, A. Urban, R. Malik and S. Kang, *Nat. Chem.*, 2016, **8**, 692–697.

14 P. Yan, J. Zheng, Z. K. Tang, A. Devaraj, G. Chen, K. Amine, J. G. Zhang, L. M. Liu and C. Wang, *Nat. Nanotechnol.*, 2019, **14**, 602–608.

15 A. J. Perez, Q. Jacquet, D. Batuk, A. Iadecola, M. Saubanère, G. Rousse, D. Larcher, H. Vezin, M. L. Doublet and J. M. Tarascon, *Nat. Energy*, 2017, **2**, 954–962.

16 J. Zheng, P. Xu, M. Gu, J. Xiao, N. D. Browning, P. Yan, C. Wang and J. G. Zhang, *Chem. Mater.*, 2015, **27**, 1381–1390.

17 K. Luo, M. R. Roberts, R. Hao, N. Guerrini, D. M. Pickup, Y. S. Liu, K. Edström, J. Guo, A. V. Chadwick, L. C. Duda and P. G. Bruce, *Nat. Chem.*, 2016, **8**, 684–691.

18 R. A. House, U. Maitra, M. A. Pérez-osorio, J. G. Lozano, L. Jin, J. W. Somerville, L. C. Duda, A. Nag, A. Walters, K. Zhou, M. R. Roberts and P. G. Bruce, *Nature*, 2019, **577**, 502–508.

19 M. D. Radin, J. Vinckeviciute, R. Seshadri and A. Van der Ven, *Nat. Energy*, 2019, **4**, 639–646.

20 P. Kalyani, S. Chitra, T. Mohan and S. Gopukumar, *J. Power Sources*, 1999, **80**, 103–106.

21 A. R. Armstrong, M. Holzapfel, P. Novák, C. S. Johnson, S. H. Kang, M. M. Thackeray and P. G. Bruce, *J. Am. Chem. Soc.*, 2006, **128**, 8694–8698.

22 A. Boulineau, L. Simonin, J. F. Colin, C. Bourbon and S. Patoux, *Nano Lett.*, 2013, **13**, 3857–3863.

23 S. Hy, F. Felix, J. Rick, W. N. Su and B. J. Hwang, *J. Am. Chem. Soc.*, 2014, **136**, 999–1007.

24 Y. Wang, Z. Yang, Y. Qian, L. Gu and H. Zhou, *Adv. Mater.*, 2015, **27**, 3915–3920.

25 M. Sathiya, A. M. Abakumov, D. Foix, G. Rousse, K. Ramesha, M. Saubanère, M. L. Doublet, H. Vezin, C. P. Laisa, A. S. Prakash, D. Gonbeau, G. VanTendeloo and J.-M. Tarascon, *Nat. Mater.*, 2015, **14**, 230–238.

26 N. Yabuuchi, K. Yoshii, S.-T. Myung, I. Nakai and S. Komaba, *J. Am. Chem. Soc.*, 2011, **133**, 4404–4419.

27 M. Gauthier, T. J. Carney, A. Grimaud, L. Giordano, N. Pour, H. H. Chang, D. P. Fenning, S. F. Lux, O. Paschos, C. Bauer, F. Maglia, S. Lupart, P. Lamp and Y. Shao-Horn, *J. Phys. Chem. Lett.*, 2015, **6**, 4653–4672.

28 R. Imhof, *J. Electrochem. Soc.*, 1999, **146**, 1702–1706.

29 J. Zheng, M. Gu, J. Xiao, P. Zuo, C. Wang and J. G. Zhang, *Nano Lett.*, 2013, **13**, 3824–3830.

30 J. Wu, X. Zhang, S. Zheng, H. Liu, J. Wu, R. Fu, Y. Li, Y. Xiang, R. Liu, W. Zuo, Z. Cui, Q. Wu, S. Wu, Z. Chen, P. Liu, W. Yang and Y. Yang, *ACS Appl. Mater. Interfaces*, 2020, **12**, 7277–7284.

31 Y. Paik, C. P. Grey, C. S. Johnson, J. S. Kim and M. M. Thackeray, *Chem. Mater.*, 2002, **14**, 5109–5115.

32 F. Sigel, B. Schwarz, K. Kleiner, C. Dräger, L. Esmezjan, M. Yavuz, S. Indris and H. Ehrenberg, *Chem. Mater.*, 2020, **32**, 1210–1223.

33 W. Hua, Z. Wu, M. Chen, M. Knapp, X. Guo, S. Indris, J. R. Binder, N. N. Bramnik, B. Zhong, H. Guo, S. Chou, Y.-M. Kang and H. Ehrenberg, *J. Mater. Chem. A*, 2017, **5**, 25391–25400.

34 M. H. Lee, T. H. Kim, Y. S. Kim and H. K. Song, *J. Phys. Chem. C*, 2011, **115**, 12255–12259.

35 W. B. Hua, X. D. Guo, Z. Zheng, Y. J. Wang, B. H. Zhong, B. Fang, J. Z. Wang, S. L. Chou and H. Liu, *J. Power Sources*, 2015, **275**, 200–206.

36 H. Yu, Y. G. So, Y. Ren, T. Wu, G. Guo, R. Xiao, J. Lu, H. Li, Y. Yang, H. Zhou, R. Wang, K. Amine and Y. Ikuhara, *J. Am. Chem. Soc.*, 2018, **140**, 15279–15289.

37 W. Hua, B. Schwarz, R. Azmi, M. Müller, M. S. Dewi Darma, M. Knapp, A. Senyshyn, M. Heere, A. Missiul, L. Simonelli, J. R. Binder, S. Indris and H. Ehrenberg, *Nano Energy*, 2020, **78**, 105231.

38 W. Hua, B. Schwarz, M. Knapp, A. Senyshyn, A. Missiul, X. Mu, S. Wang, J. R. Binder, S. Indris and H. Ehrenberg, *J. Electrochem. Soc.*, 2019, **166**, 5025–5032.

39 R. Baddour-hadjean, *Chem. Rev.*, 2010, **110**, 1278–1319.

40 M. H. Lin, J. H. Cheng, H. F. Huang, U. F. Chen, C. M. Huang, H. W. Hsieh, J. M. Lee, J. M. Chen, W. N. Su and B. J. Hwang, *J. Power Sources*, 2017, **359**, 539–548.

41 M. C. Biesinger, B. P. Payne, A. P. Grosvenor, L. W. M. Lau, A. R. Gerson and R. S. C. Smart, *Appl. Surf. Sci.*, 2011, **257**, 2717–2730.

42 R. Azmi, V. Trouillet, M. Strafela, S. Ulrich, H. Ehrenberg and M. Bruns, *Surf. Interface Anal.*, 2018, **50**, 43–51.

43 X. Li, Y. Qiao, S. Guo, Z. Xu, H. Zhu, X. Zhang, Y. Yuan, P. He, M. Ishida and H. Zhou, *Adv. Mater.*, 2018, **30**, 1705197.

44 W. Yin, A. Grimaud, G. Rousse, A. M. Abakumov, A. Senyshyn, L. Zhang, S. Trabesinger, A. Iadecola, D. Foix, D. Giaume and J. M. Tarascon, *Nat. Commun.*, 2020, **11**, 1252.

45 L. de Biasi, B. Schwarz, T. Brezesinski, P. Hartmann, J. Janek and H. Ehrenberg, *Adv. Mater.*, 2019, **31**, 1900985.

46 W. Hua, K. Wang, M. Knapp, B. Schwarz, S. Wang, H. Liu, M. Müller, A. Schökel, A. Missyul, D. F. Sanchez, X. Guo, J. R. Binder, J. Xiong, S. Indris and H. Ehrenberg, *Chem. Mater.*, 2020, **32**, 4984–4997.

47 D. Eum, B. Kim, S. J. Kim, H. Park, J. Wu, S. P. Cho, G. Yoon, M. H. Lee, S. K. Jung, W. Yang, W. M. Seong, K. Ku, O. Tamwattana, S. K. Park, I. Hwang and K. Kang, *Nat. Mater.*, 2020, **19**, 419–427.

48 Z. Zhu, D. Yu, Y. Yang, C. Su, Y. Huang, Y. Dong, I. Waluyo, B. Wang, A. Hunt, X. Yao, J. Lee, W. Xue and J. Li, *Nat. Energy*, 2019, **4**, 1049–1058.

49 R. Chen, S. Ren, M. Knapp, D. Wang, R. Witter, M. Fichtner and H. Hahn, *Adv. Energy Mater.*, 2015, **5**, 1–7.

50 J. Lee, A. Urban, X. Li, D. Su, G. Hautier and G. Ceder, *Science*, 2014, **343**, 519–522.